# *k*- and Doppler Velocity Decomposition-Based Range Points' Migration for 3-D Localization With Millimeter Wave Radar

Takeru Ando and Shouhei Kidera , *Senior Member, IEEE*

Abstract—A *k*-space and Doppler velocity decomposition based on an accurate millimeter wave (mmW) 3-D target localization method is presented, using the range points' migration (RPM) method to provide multi-information associated with point clouds. The incoherent method, known as RPM, has a number of advantages over coherent localization, including avoiding a false response due to phase uncertainty or the necessity for highly accurate phase calibration in multiple arrays. However, various concerns must be addressed to retain the benefit of high-frequency mmW radar. In order to bring some benefits of high-frequency mmW radar into RPM scheme, this study introduces the *k*-space and Doppler velocity decomposition schemes for multiple objects moving at different speeds into the RPM scheme, where a new weighted term is introduced. In addition, the RPM point cloud is incorporated with the incoherent Doppler velocity estimation method known as the weighted kernel density (WKD) method, which provides a multifunctional 3-D localization. The mmW radar experiment in the 79-GHz band demonstrates that our proposed method achieves accurate 3-D Doppler-associated localization, even with a small aperture array.

Index Terms— Doppler-associated localization, millimeter wave (mmW) radar, point cloud 3-D localization, radar signal processing.
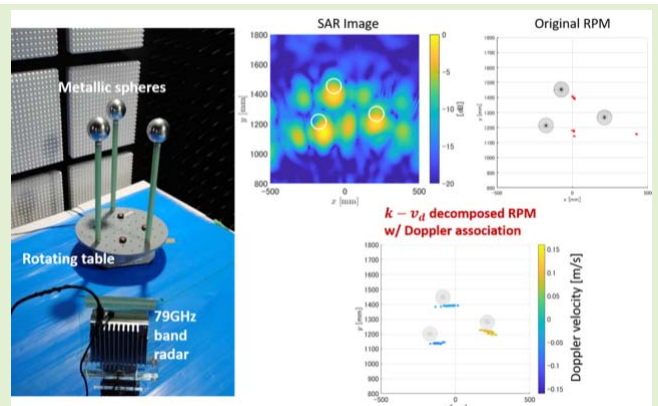
I. INTRODUCTION

THERE is a high demand for environmentally robust sensing tools in various short-sensing scenes. In particular, millimeter wave (mmW) radars are one of the promising sensing techniques [1], [2], as they are applicable to severe sensing conditions, such as optically blurred conditions or nonline-of-sight conditions [3]. However, a moderate spatial resolution is critical to reconstructing an accurate image of a complex shape, such as the human body, even when using a higher frequency band, such as the over 70-GHz band [4], [5], [6], [7] due to interference from multiple scattering centers on multiple objects, which is also downgraded by the radar module's limited aperture size. There are many studies for the 3-D radar imaging scheme, the majority of which are based

on coherent integration (CI) methods, such as synthetic aperture radar (SAR) [8], [9], Kirchhoff migration approaches [10], [11], or the range migration algorithm (RMA) [12], [13], [14], [15], [16] where a higher azimuth resolution is obtained via a coherent process.

Nonetheless, the aforementioned methods suffer from unnecessary responses due to speckle noise or grating lobe effects when an array alignment or phase calibration is not completely adjusted or sparse array configuration. Recently, to accommodate more flexible array configurations, a sparse regularization-based algorithm dubbed "compressed sensing (CS)" has been developed, and a number of papers have demonstrated that it retains an image as accurate as that obtained using fully distributed array data [18], [19], [20]. However, it requires a high computational cost and a high signal-to-noise ratio (SNR) level. As lower complexity algorithms, the low rank matrix recovery algorithms, e.g., singular value thresholding (SVT) [21] and principal component pursuit using the alternating directions method (PCPADM) [22], have been developed. However, as demonstrated in a previous study [23], the CS schemes would suffer from inaccuracy due to random noise. In addition, deep learning schemes, such as complex-valued convolutional neural networks, are applied in

The authors are with the Graduate School of Informatics and Engineering, The University of Electro-Communications, Tokyo 182-8585, Japan (e-mail: kidera@uec.ac.jp).

the low complexity CS approach [24]; however, they require a sufficient number of training data.

As a promising countermeasure to the aforementioned issue, some incoherent localization methods have been developed, some of which exploit the time-of-flight (TOF) conversion. Among these, the range points' migration (RPM) method has a number of advantages [25], such as low complexity, a simple algorithm, noise robustness, and multifunctional feature association. The RPM converts the TOF, referred to as the range point (RP) (defined as the TOF associated with the transmitter and receiver locations), to each associated scattering center on the object surface using a weighted Gaussian kernel density estimator generated by a number of RPs observed at different locations. A distinct feature of the RPM is that it avoids complicated preprocessing about the connection or tracking of multiple RPs, which is known as a joint problem when processing multiple TOF values. The accuracy of RPM is determined by the bandwidth, not the carrier frequency. In using a 79-GHz band mmW system, we obtain 4-GHz bandwidth, namely, 37.5-mm range resolution; however, there are some cases where this range resolution is still insufficient for closely located multiple targets with motion. To address this issue, Akiyama et al. [26] introduced k-space decomposition, i.e., wavenumber spectrum analysis with array data in the RPM imaging scheme to decompose reflections from multiple objects, but it suffers from inaccuracy due to an insufficient resolution in k-space caused by the limited aperture size.

To address the aforementioned problem, this study introduces not only k-space but the Doppler velocity decomposition scheme into the RPM method, which is specified for multiple objects with different motions, such as the human body in walking motion. Focusing on the Doppler velocity data, although several studies have reported solving a phase compensation problem due to Doppler velocity variance or high-speed motion object, to retain the original range-Doppler estimation performance [27], [28], [29], there are few studies on enhancing the imaging accuracy using the Doppler velocity-based data decomposition, e.g., [16], [30], and [31]. In particular, a Doppler and range cell migration has been employed to retain both range and Doppler velocity resolutions [30], but the prior estimation of target motion and position to compensate for the Doppler velocity variance was required. Ram and Majumdar [31] enhanced the spatial resolution of a radar image by exploiting the Doppler velocity difference among human body parts in walking motion; nonetheless, the CS imaging scheme, which requires much complexity in 3-D imaging scenarios, was employed. Ohmori and Kidera [16] also introduced a similar method for the RMA scheme, but it is based on the CI processing, requiring a dense array configuration and resulting in some speckle noise or sidelobe responses due to CI processing. In addition, in the RPM imaging scheme, Sasaki et al. [17] introduced Doppler-associated RPM imaging for human body motion, but only the Doppler velocity decomposition was introduced, i.e., k-space decomposition was not implemented. As the novelty of this article, the reflection responses are decomposed not only in k-space but also in Doppler velocity space, via a 4-D Fourier transform (FFT) scheme across both spatial

(transmitter and receiver region) and temporal (slow time) domains, to maintain an imaging accuracy. In addition, the incorporation examples of the RPM and the weighted kernel density (WKD) method [34] are presented to provide not only accurate 3-D localization but also associated Doppler velocity, that is, multifunctional localization. In this scheme, each scattering center point provided by the RPM could be associated with Doppler velocity provided by the WKD method, which is also based on the incoherent RPs' conversion, and the $k - v_{\mathrm{d}}$ decomposed WKD method has also been presented in [23]. Note that, since both RPM and WKD methods deal with the incoherent conversion of a slow time-associated RP (called range-τ point), they are suitable for providing Doppler-associated 3-D localization with high temporal resolution. In addition, while the RPM uses an incoherent process, the $k - v_{\mathrm{d}}$ decomposition is based on a coherent process to provide the advantages of higher cross-range resolution and noise robustness. It should be noted that the literature [35] incorporates the RPM and WKD; however, it only deals with the 2-D problem and does not include k-Doppler decomposition, that is, it is not suitable for the mmW radar model. Another contribution of this study, the RPM algorithm is modified to be suitable for $k - v_{\mathrm{d}}$ decomposition data, where the constrained weights as to k-space proximity are also implemented to avoid the deviation of RPM localization points.

In summarize, the main contributions of this study are listed as follows.

1) In the range-τ point extraction process, k and v_{d} space decomposition could isolate a spectrum ascribed to each target location and help to suppress false detection due to sidelobes or interfering responses from targets with different locations.

2) The k and v_{d} data decomposition scheme is first introduced into the RPM imaging scenario, which has been validated via the experimental data using the 79-GHz multiple-input–multiple-output (MIMO) mmW radar module.

3) The k-space weighted RPM scheme further improves the reconstruction accuracy by avoiding a false response due to a coherent process, and the 4-D FFT scheme reduces the computational complexity.

4) Multifunctional point clouds associated with Doppler velocity are achieved by exploiting the distinct feature of RPM and WKD, which could not be achieved by major CI techniques.

The experimental validations were performed using 79-GHz ultrawideband radar with MIMO configuration for the case of three rotating metallic spheres, where the time-variant Doppler velocity and 3-D target localization can be assessed quantitatively.

II. METHOD

A. Observation Model

Fig. 1 illustrates the observation model assumed in this study. A number of transmitters and receivers are located on the plane of $y = 0$, configuring the 2-D array. Here, $L^{\mathrm{T}} = (x_T, 0, z_T)$ and $L^{\mathrm{R}} = (x_R, 0, z_R)$ are defined as
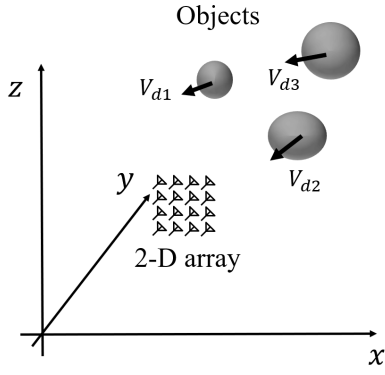
Fig. 1. Observation model.

the locations of the transmitter and the receiver, respectively. It assumes multiple objects with different velocity vectors, which are variable in the total observation time. This assumption applies to an object such as a human body motion, a bicycle, or another low-speed object. In a data acquisition sequence, each transmitter recursively transmits pulses or frequency-modulated signals with a fixed pulse repetition interval (PRI). τ is defined as each pulse hit sequence, which is called slow time. $s(L^{\mathrm{T}}, L^{\mathrm{R}}, R', \tau)$ is defined as the recorded complex-valued signals at the specific combination of the transmitter and the receiver, where $R' = \mathrm{c}t/2$ is defined with the fast time t and the propagation speed c. Here, when assuming a specific filter, such as a matched filter, $\tilde{s}(L^{\mathrm{T}}, L^{\mathrm{R}}, R', \tau)$ is defined as its response. A discrete range-τ point, defined as $q \equiv (L^{\mathrm{T}}, L^{\mathrm{R}}, R, \tau)$, is extracted from the local peaks of $|\tilde{s}(L^{\mathrm{T}}, L^{\mathrm{R}}, R', \tau)|$ along the R-direction as

$$\frac{\partial |\tilde{s}(L^{\mathrm{T}}, L^{\mathrm{R}}, R', \tau)|}{\partial R'} = 0 \quad (1)$$

$$\left| \tilde{s}(L^{\mathrm{T}}, L^{\mathrm{R}}, R', \tau) \right| \geq \alpha \max_{R', \tau} \left| \tilde{s}(L^{\mathrm{T}}, L^{\mathrm{R}}, R', \tau) \right| \quad (2)$$

where α is the threshold and holds $0 \leq \alpha \leq 1$. Note that, in the monostatic model, R in $q \equiv (L^{\mathrm{T}}, L^{\mathrm{R}}, R, \tau)$ indicates the one-way distance from a sensor location point to a target boundary point (reflection point). It should be noted that a frequency-modulated continuous-wave (FMCW) radar system is also applicable if a complex-valued filter response $\tilde{s}(L^{\mathrm{T}}, L^{\mathrm{R}}, R', \tau)$ is observable. Each range-τ point could be associated with each scattering center on a target boundary, which is also variant to slow time τ.

B. Coherent Integration-Based Imaging

The majority of radar imaging methods, such as synthetic aperture, the Kirchhoff migration, or RMA, is based on CI. As a distinct advantage of CI, it provides high azimuth and elevation resolutions when used in conjunction with high-frequency radar, such as mmW radar, or a significant noise reduction effect due to CI. However, the CI method usually generates unnecessary responses due to the speckle noise, sidelobe, or grating lobe effect. The array spacing should be less than a half-wavelength of the carrier wavelength, which limits the dimension of the antenna structure and requires accurate synchronization among a number of transmitters and receivers.

C. RPM Method

1) Original RPM Algorithm: The RPM method was developed to address the above issues inherent in the CI-based method. The RPM is based on incoherent conversions of observed range-τ points q to their associated scattering centers represented by $p(q)$ on the target surface. The methodology of RPM is described as follows. A scattering center point $p(q)$ should exist on a spheroid with foci of L^{T} and L^{R} and a semimajor axis R according to the high-frequency approximation, namely, the geometrical optics (GO) model. In addition, an actual scattered center is located around the area, where the intersection points determined by different $p(q)$ are accumulated. However, since a calculation of the intersection point of the three spheroids is computationally complicated, the sampled point-based RPM algorithm [36] is introduced to reduce the complexity. It determines the scattering center by focusing on the ith range-τ point at the jth pulse hit τ_j as $q_{i,j}$

$$\hat{p}(q_{i,j}) = \arg \max_{p_k^{\mathrm{g}}(q_{i,j})} \sum_{q_{i,l} \in \mathcal{Q}_{all}} s(q_{i,l}) \exp\left\{ -\frac{D(q_{i,j}, q_{i,l})^2}{2\sigma_D^2} \right\}$$
$$\times \exp\left\{ -\frac{L(p_k^{\mathrm{g}}(q_{i,j}), q_{i,l})^2}{2\sigma_L^2} \right\}. \quad (3)$$

$p_k^{\mathrm{g}}(q_{i,j})$ denotes the kth sampled point on the above spheroid obtained from $q_{i,j}$, and is given as

$$p_k^{\mathrm{g}}(q_{i,j}) = \left(L_{i,j}^{\mathrm{T}} + L_{i,j}^{\mathrm{R}} \right)/2$$
$$+ R_{i,j} (\sin \theta_k \cos \psi_k, \cos \theta_k, \sin \theta_k \sin \psi_k). \quad (4)$$

$D(q_{i,j}, q_{i,l})$ denotes the actual separation of the two sets of transmitting and receiving antennas as

$$D(q_{i,j}, q_{i,l}) = \min\left(\left\| L_{i,j}^{\mathrm{T}} - L_{i,l}^{\mathrm{T}} \right\|^2 + \left\| L_{i,j}^{\mathrm{R}} - L_{i,l}^{\mathrm{R}} \right\|^2 \right.$$
$$\left. \left\| L_{i,j}^{\mathrm{T}} - L_{i,l}^{\mathrm{R}} \right\|^2 + \left\| L_{i,j}^{\mathrm{R}} - L_{i,l}^{\mathrm{T}} \right\|^2 \right). \quad (5)$$

σ_D is the constant parameter, considering the correlation length along a sensor location. Also, the term $L(p_k^{\mathrm{g}}(q_{i,j}), q_{i,l})$ is defined as

$$L(p_k^{\mathrm{g}}(q_{i,j}), q_{i,l}) \equiv \left| \left\| L_{i,l}^{\mathrm{T}} - p_k^{\mathrm{g}}(q_{i,j}) \right\| \right.$$
$$\left. + \left\| L_{i,l}^{\mathrm{R}} - p_k^{\mathrm{g}}(q_{i,j}) \right\| - 2R_{i,j} \right|/2. \quad (6)$$

$L(p_k^{\mathrm{g}}(q_{i,j}), q_{i,l})$ is introduced by assessing the distance from the intersection points to the sample point on the assumed spheroid, the details of which are explained in [36]. Since σ_L expresses the spatial variations of the intersection points, it is usually set to a sufficiently smaller value than the array interval. σ_D determines the correlation length along element location and should be set to a couple of intervals of arrays. There are detailed discussions of these parameters [25], [36]. Fig. 2 shows the 2-D simplified illustration for the intersection of the spheroids (ellipsoidal cross section in the 2-D model) and the scattering center point $\hat{p}(q_{i,j})$. As shown in the figure, the sampled grid points $p_k^{\mathrm{g}}(q_{i,j})$ are defined as points on the
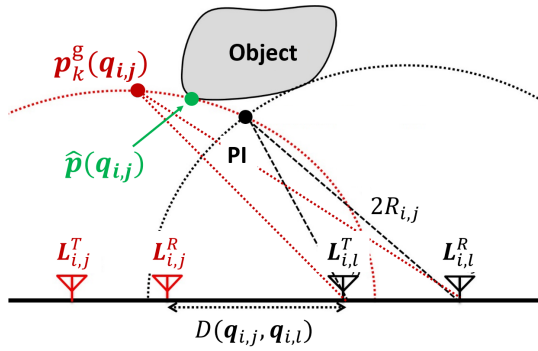
Fig. 2. 2-D illustration of the relationship among locations of transmitter and receivers, the intersection points of spheroids, and the scattering center point. The sampled point $p_k^g(q_{i,j})$ should be on the circumference of the ellipse defined with $q_{i,j}$.
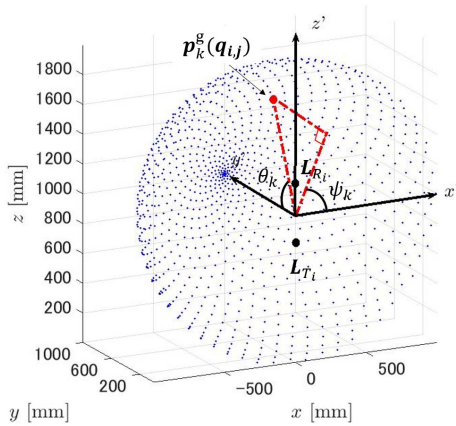

Fig. 3. Distribution of sampled points with golden ratio patterns and the definitions of the azimuth and elevation angles for each sample point.

circumference of a spheroid (ellipse), with the foci of $L_{i,j}^T$ and $L_{i,j}^R$ and a semimajor axis $R_{i,j}$ defined with the focused range-τ point ($q_{i,j}$). In this algorithm, it assumes that the distance $L(p_k^g(q_{i,j}))$ becomes a promising metric for calculating the distance from the intersection point to the grid points $p_k^g(q_{i,j})$, which considerably reduces the computational complexity in the RPM process.

In particular, as an efficient sampling pattern of sampled point $p_k^g(q_{i,j})$, the golden ratio is implemented as [36]

$$\theta_k = (k-1)\pi/2M, \tag{7}$$
$$\psi_k = 4(k-1)\pi/M\left(1+\sqrt{5}\right). \tag{8}$$

This algorithm has been demonstrated to provide both accurate and low complexity 3-D imaging for elaborately shaped targets, such as the human body [36]. Fig. 3 shows the 3-D distribution of the sampled points using the above golden ratio pattern.

Note that, since the RPM converts each range-τ point to its associated scattering center using the incoherent process in (3), it completely avoids an unnecessary response due to the sidelobe, grating lobe, or speckle effect. In addition, the RPM could provide a significant noise reduction effect, by eliminating falsely estimated scattered center points with

the lower evaluation values maximized in (3). Nonetheless, the RPM cannot obtain the advantage of higher carrier frequency systems, namely, a higher azimuth resolution using an array configuration. This is because the accuracy of RPM reconstruction largely depends on the available range resolution. For example, if we obtain accurate range-τ points (TOF profiles) in the presence of the interference of multiple targets, the RPM provides a highly accurate point cloud for target localization, as shown in [25]. Furthermore, as the RPM does not introduce a coherent process along the cross-range direction, its cross-range resolution could not be clearly defined. The accuracy of the RPM imaging, including the along cross-range direction, is directly affected by the accuracy of the obtained TOFs, which are determined by the SNR and the range resolution when assuming multiple objects. Specifically, if we assume a symmetrical structure with an equal distance from the center of the array, only one local peak would be extracted in (10) because of the limitation of range resolution, and we cannot reconstruct separated target images using the RPM scheme. Incorporation of super-resolution TOF techniques, such as the Capon method [50] or CS [34], would offer one promising solution for the abovementioned problem. However, it requires high S/N ratios and expensive computational complexity. The literature [26] introduced the k-space decomposition to retain high-resolution 3-D imaging using the RPM scheme. However, it still suffers from inaccuracy in the case of limited aperture size.

2) Doppler and k-Space Decomposition-Based RPM: To address the aforementioned issue, this study proposes a k and Doppler velocity space decomposition scheme for enhancing the accuracy of RPM localization. This approach is motivated by the well-established fact that, even if multiple objects exist within the range resolution, such as symmetric shape, the direction of arrivals (DOA) or Doppler velocity could be different in some cases. The proposed scheme employs a k-v_d space decomposition to suppress false detection in extracting the range-τ points, which are caused by sidelobe or other interfering responses ascribed to targets with different locations. This decomposition scheme has been introduced in the accurate Doppler velocity estimation issue [23] using the Fourier transform of the observed data; however, it was not introduced to the localization issues for multiple targets.

First, we describe the above decomposition scheme. It is assumed that a reflection response at each sensor contains multiple reflections from objects with different DOAs and velocities. Thus, the data decomposition would be advantageous not only in k-space (the DOA space) like [26] but also in Doppler velocity space. As a distinct advantage of this method, this decomposition could be implemented by the 4-D Fourier transform as

$$S\left(k_x, k_z, k_R, v_d; \boldsymbol{L}^T\right)$$
$$= \iint_A \int_T \int_{\mathcal{R}} \tilde{s}\left(\boldsymbol{L}^T, x_R, z_R, R, \tau\right)$$
$$\times e^{-j(k_x x_R + k_z z_R + k_R R + \omega\tau)} dx_R dz_R dR d\tau \tag{9}$$

where A denotes the aperture area, and k_R, k_x, and k_z are the wavenumbers of R, x_R, and z_R, respectively. T and $\mathcal{R}$

denote the integration period along τ and R, respectively, and $v_{\mathrm{d}} = \omega\lambda/4\pi$ holds. Focusing on the specific $k_R = k_{\mathrm{CR}}$, determined by the center frequency of the transmitted pulse, $\boldsymbol{\zeta}^{(n)} \equiv (\tilde{k}_x^{(n)}, \tilde{k}_z^{(n)}, v_{\mathrm{d}}^{(n)})$ is extracted from the local maxima of $S(k_x, k_z, k_{\mathrm{CR}}, v_{\mathrm{d}}; \boldsymbol{L}^T))$ as

$$
\left.\begin{array}{r}
\partial \left| S\left(k_x, k_z, k_{\mathrm{CR}}, v_{\mathrm{d}}; \boldsymbol{L}^T\right) \right| / \partial k_x = 0 \\
\partial \left| S\left(k_x, k_z, k_{\mathrm{CR}}, v_{\mathrm{d}}; \boldsymbol{L}^T\right) \right| / \partial k_z = 0 \\
\partial \left| S\left(k_x, k_z, k_{\mathrm{CR}}, v_{\mathrm{d}}; \boldsymbol{L}^T\right) \right| / \partial v_{\mathrm{d}} = 0 \\
\left| S\left(k_x, k_z, k_{\mathrm{CR}}, v_{\mathrm{d}}; \boldsymbol{L}^T\right| \right. \\
\geq \beta \max_{k_x, k_z, v_{\mathrm{d}}} \left| S\left(k_x, k_z, k_{\mathrm{CR}}, v_{\mathrm{d}}; \boldsymbol{L}^T\right) \right|)
\end{array}\right\} \quad (10)
$$

where n denotes the index number of local maxima. β denotes the threshold parameter. It should be noted that, if β is not sufficiently small, there is a possibility to miss a target response with relatively weaker local peaks in k_x-k_z-v_{d} space. However, as the k_x, k_z, and v_{d} decomposition scheme is based on a CI process, random noise components could not be considerably suppressed. Thus, we could set parameter β sufficiently small to avoid missing targets with lower reflectivity to some extent.

It is considered that the decomposed data around the extracted $\boldsymbol{\zeta}^{(n)}$ would contain only the reflection data from the specific DOA ($\tilde{k}_x^{(n)}$ and $\tilde{k}_z^{(n)}$) or the Doppler velocity $v_{\mathrm{d}}^{(n)}$. Then, the reflection response $S(k_x, k_z, k_R, v_{\mathrm{d}}; \boldsymbol{L}^T)$ is calculated via the following 4-D inverse Fourier transform as:

$$
\begin{aligned}
&\tilde{s}\left(\boldsymbol{L}^T, \boldsymbol{L}^R, R, \tau; \boldsymbol{\zeta}^{(n)}\right) \\
&= \frac{1}{16\pi^4} \iiiint W\left(k_x, k_z, v_{\mathrm{d}}; \boldsymbol{\zeta}^{(n)}\right) S\left(k_x, k_z, k_R, v_{\mathrm{d}}; \boldsymbol{L}^T\right) \\
&\quad \times e^{j(k_x x_R + k_z z_R + k_R R + \omega\tau)} dk_x dk_z dk_R d\omega.
\end{aligned} \quad (11)
$$

$W(k_x, k_z, v_{\mathrm{d}}; \boldsymbol{\zeta}^{(n)})$ is the window function in k_x-k_z-v_{d} space, such as the multidimensional Gaussian function. The span of $W(k_x, k_z, v_{\mathrm{d}}; \boldsymbol{\zeta}^{(n)})$ should be set as each resolution of k_x, k_z, and v_{d}, which could be determined by the aperture angle and coherent processing interval (CPI) with the center wavelength. Using the nth clustered decomposed data $\tilde{s}(\boldsymbol{L}^T, \boldsymbol{L}^R, R, \tau; \boldsymbol{\zeta}^{(n)})$, the range-$\tau$ points are updated from each cluster as $\tilde{\boldsymbol{q}}_{i,j}^{(n)} \equiv (\boldsymbol{L}_{i,j}^{\mathrm{T},(n)}, \boldsymbol{L}_{i,j}^{\mathrm{R},(n)}, R_{i,j}^{(n)}, \tau_i^{(n)})$ under the following condition:

$$
\frac{\partial \left| \tilde{s}\left(\boldsymbol{L}^T, \boldsymbol{L}^R, R, \tau; \boldsymbol{\zeta}^{(n)}\right) \right|}{\partial R} = 0 \quad (12)
$$

$$
\left| \tilde{s}\left(\boldsymbol{L}^T, \boldsymbol{L}^R, R, \tau; \boldsymbol{\zeta}^{(n)}\right) \right| \geq \alpha \max_{R, \tau} \left| \tilde{s}\left(\boldsymbol{L}^T, \boldsymbol{L}^R, R, \tau; \boldsymbol{\zeta}^{(n)}\right) \right| \quad (13)
$$

where α is the threshold parameter, which holds $0 \leq \alpha \leq 1$. Note that the above decomposition process is achieved by the 4-D FFT and inverse FFT (IFFT) processes, which achieves a low computational cost, compared with the other filtering methods, e.g., CS or Capon.

D. k-Space-Constrained RPM

In the case of a narrow array or synthetic aperture, the original RPM has an inherent problem in that its accuracy is highly sensitive to range-τ point error. This study also introduces the k-space weighted RPM algorithm to maintain a reconstruction

accuracy, even with a narrow aperture. As a notable point of the above decomposition scheme, the representative elevation and azimuth angles, derived from $\tilde{k}_x^{(n)}$ and $\tilde{k}_z^{(n)}$, are solely associated with the range-τ point as $\tilde{\boldsymbol{q}}_{i,j}^{(n)}$. This association is formulated as follows. Here, $\phi^{(n)}$ and $\theta^{(n)}$ are defined as the azimuth and elevation angles, respectively, calculated from the associated wavenumber as $\tilde{k}_x^{(n)}$ and $\tilde{k}_z^{(n)}$ using the following relationship:

$$
\phi^{(n)} = \sin^{-1}\left(\frac{k_x^{(n)}\lambda}{2\pi}\right) \quad (14)
$$

$$
\theta^{(n)} = \sin^{-1}\left(\frac{k_z^{(n)}\lambda}{2\pi}\right). \quad (15)
$$

Also, the associated range $R^{(n)}$ is calculated as

$$
\begin{aligned}
R^{(n)} = \arg \max_R \frac{1}{2\pi} \int W\left(k_x, k_z, v_{\mathrm{d}}; \boldsymbol{\zeta}^{(n)}\right) \\
\times S\left(k_x, k_z, k_R, v_{\mathrm{d}}; \boldsymbol{L}^T\right) e^{j(k_R R)} dk_R. \quad (16)
\end{aligned}
$$

Then, the associated Cartesian coordinates defined as $(x^{(n)}, y^{(n)}, z^{(n)})$ are calculated as $x^{(n)} = X_{\mathrm{C}} + R^{(n)} \cos\theta^{(n)} \sin\phi^{(n)}$, $y^{(n)} = Y_{\mathrm{C}} + R^{(n)} \cos\theta^{(n)} \cos\phi^{(n)}$, and $z^{(n)} = Z_{\mathrm{C}} + R^{(n)} \sin\theta^{(n)}$, respectively, where $(X_{\mathrm{C}}, Y_{\mathrm{C}}, Z_{\mathrm{C}})$ denotes the location of the array center. Then, $\theta(\tilde{\boldsymbol{q}}_{i,j}^{(n)})$ and $\phi(\tilde{\boldsymbol{q}}_{i,j}^{(n)})$ solely associated as $\tilde{\boldsymbol{q}}_{i,j}^{(n)}$ are expressed as

$$
\phi\left(\tilde{\boldsymbol{q}}_{i,j}^{(n)}\right) = \tan^{-1}\left(\frac{x^{(n)} - x_{i,j}^{\mathrm{TR}}}{y^{(n)}}\right) \quad (17)
$$

$$
\theta\left(\tilde{\boldsymbol{q}}_{i,j}^{(n)}\right) = \sin^{-1}
$$
$$
\times \left(\frac{z^{(n)} - z_{i,j}^{\mathrm{TR}}}{\sqrt{\left(x^{(n)} - x_{i,j}^{\mathrm{TR}}\right)^2 + \left(y^{(n)}\right)^2 + \left(z^{(n)} - z_{i,j}^{\mathrm{TR}}\right)^2}}\right) \quad (18)
$$

where $x_{i,j}^{\mathrm{TR}} = (x_{\mathrm{T},i,j} + x_{\mathrm{R},i,j}/2)$ and $z_{i,j}^{\mathrm{TR}} = (z_{\mathrm{T},i,j} + z_{\mathrm{R},i,j}/2)$ hold. The scattering center point associated with $\tilde{\boldsymbol{q}}_{i,j}^{(n)}$ is determined as

$$
\begin{aligned}
&\hat{\boldsymbol{p}}\left(\boldsymbol{q}_{i,j}\right) \\
&= \arg \max_{\boldsymbol{p}_k^{\mathrm{g}}(\boldsymbol{q}_{i,j})} \sum_{\boldsymbol{q}_{i,l} \in \mathcal{Q}_{all}} s\left(\boldsymbol{q}_{i,l}\right) \\
&\quad \times \exp\left\{-\frac{D\left(\boldsymbol{q}_{i,j}, \boldsymbol{q}_{i,l}\right)^2}{2\sigma_D^2}\right\} \exp\left\{-\frac{L\left(\boldsymbol{p}_k^{\mathrm{g}}\left(\boldsymbol{q}_{i,j}\right), \boldsymbol{q}_{i,l}\right)^2}{2\sigma_L^2}\right\} \\
&\quad \times \exp\left\{-\frac{\Theta\left(\boldsymbol{p}_k^{\mathrm{g}}\left(\boldsymbol{q}_{i,j}\right), \boldsymbol{q}_{i,l}\right)^2}{2\sigma_\theta^2} - \frac{\Phi\left(\boldsymbol{p}_k^{\mathrm{g}}\left(\boldsymbol{q}_{i,j}\right), \boldsymbol{q}_{i,l}\right)^2}{2\sigma_\phi^2}\right\} \quad (19)
\end{aligned}
$$

where $\Theta(\boldsymbol{p}_k^{\mathrm{g}}(\boldsymbol{q}_{i,j}), \boldsymbol{q}_{i,l})$ and $\Phi(\boldsymbol{p}_k^{\mathrm{g}}(\boldsymbol{q}_{i,j}), \boldsymbol{q}_{i,l})$ are defined as

$$
\Theta\left(\boldsymbol{p}_k^{\mathrm{g}}\left(\boldsymbol{q}_{i,j}\right), \boldsymbol{q}_{i,l}\right) \equiv \left| \theta\left(\boldsymbol{p}_k^{\mathrm{g}}\left(\boldsymbol{q}_{i,j}\right)\right) - \theta\left(\tilde{\boldsymbol{q}}_{i,j}^{(n)}\right) \right| \quad (20)
$$

$$
\Phi\left(\boldsymbol{p}_k^{\mathrm{g}}\left(\boldsymbol{q}_{i,j}\right), \boldsymbol{q}_{i,l}\right) \equiv \left| \phi\left(\boldsymbol{p}_k^{\mathrm{g}}\left(\boldsymbol{q}_{i,j}\right)\right) - \phi\left(\tilde{\boldsymbol{q}}_{i,j}^{(n)}\right) \right|. \quad (21)
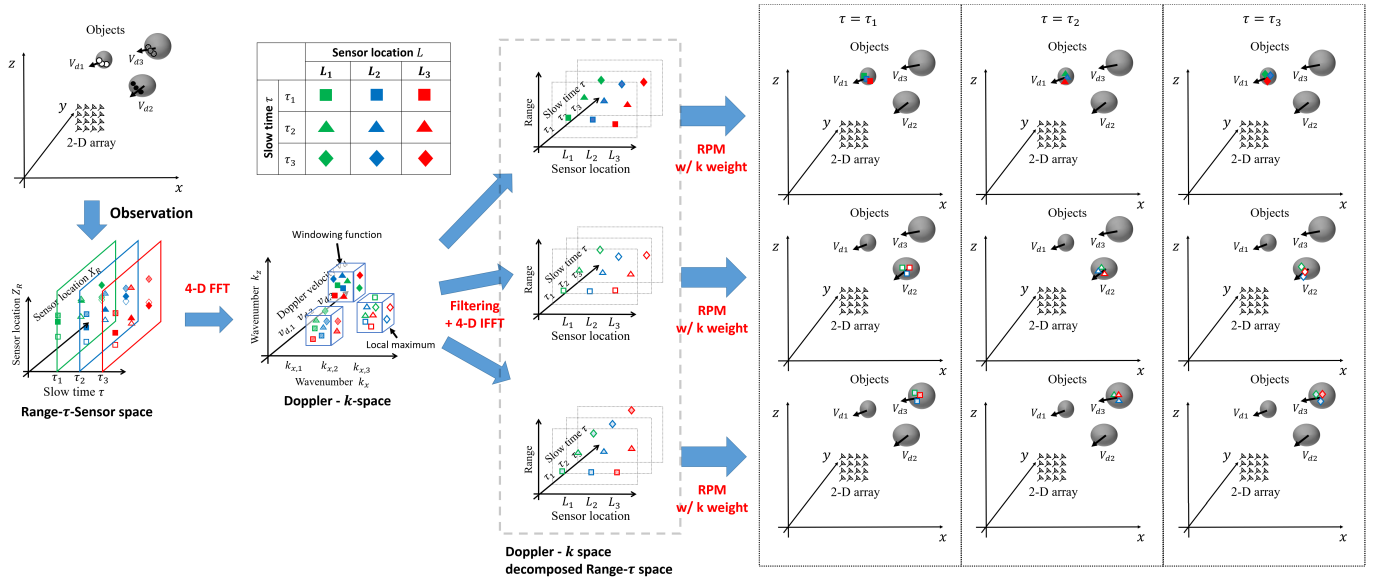$$

Fig. 4. Schematic of the proposed methodology, especially for 4-D Fourier transform-based data decomposition and *k*-space-constrained RPM.

This weighting process can suppress unnecessary deviation of the RPM point clouds because each point must be constrained to the associated DOA area using $\theta(\tilde{\boldsymbol{q}}_{i,j}^{(n)})$ and $\phi(\tilde{\boldsymbol{q}}_{i,j}^{(n)})$, which is obtained via the CI process.

Fig. 4 shows the schematic illustration of the proposed methodology, described above. As a notable advantage of this method, it decomposes the richly interfered reflection data along both *k*-space and Doppler velocity spaces, via the 4-D FFT scheme, and it significantly enhances the extraction accuracy of the range-τ points. While the decomposition scheme is based on a coherent process, the localization process, i.e., the conversion from range-τ point to scattered center point, is still incoherent, and it can avoid an ambiguous sidelobe effect generated by the CI approach. Thus, the proposed method has the advantages of coherent and incoherent schemes in terms of higher frequency-based resolution or noise-robustness enhancement via the *k*- and Doppler-velocity space and a false response reduction effect. Furthermore, the RPM does not need the preliminary allocations of the region of interest unlike the CI approach, and then, this approach has a definitive advantage in terms of computational cost when the target position is completely unknown.

E. Processing Flow

The procedure of the proposed method, namely, k-v_{d} decomposed-based RPM with k constraint, is summarized as follows.

Step 1: The measured signal $s(\boldsymbol{L}^{\mathrm{T}}, \boldsymbol{L}^{\mathrm{R}}, R, \tau)$ at each slow-time τ is sequentially processed by the matched filter at all combinations of transmitters and receivers. The above filter responses are expressed as $\tilde{s}(\boldsymbol{L}^{\mathrm{T}}, \boldsymbol{L}^{\mathrm{R}}, R, \tau)$.

Step 2: At the specific slow time τ_i, the part of $\tilde{s}(\boldsymbol{L}^{\mathrm{T}}, \boldsymbol{L}^{\mathrm{R}}, R, \tau)$ is extracted within the CPI as T, denoted as $\tilde{s}(\boldsymbol{L}^{\mathrm{T}}, \boldsymbol{L}^{\mathrm{R}}, R, \tau; \tau_i)$, where the center of CPI is set to τ_i.

Step 3: $\tilde{s}(\boldsymbol{L}^{\mathrm{T}}, \boldsymbol{L}^{\mathrm{R}}, R, \tau; \tau_i)$ are transformed to $S(k_x, k_z, k_R, v_{\mathrm{d}}; \boldsymbol{L}^T, \tau_i)$ via the 4-D Fourier transform as in (9).

Step 4: $\boldsymbol{\zeta}^{(n)}$ are extracted from local maxima of $S(k_x, k_z, k_R, v_{\mathrm{d}}; \boldsymbol{L}^T, \tau_i)$ in (10). $\tilde{s}(\boldsymbol{L}^T, \boldsymbol{L}^R, R, \tau; \boldsymbol{\zeta}^{(n)}, \tau_i)$ is extracted in the filtering process in (11).

Step 5: From each $\tilde{s}(\boldsymbol{L}^T, \boldsymbol{L}^R, R, \tau; \boldsymbol{\zeta}^{(n)}, \tau_i)$, range-$\tau$ point $\tilde{\boldsymbol{q}}_{i,j}^{(n)}$ is in (13).

Step 6: For all range-τ points $\tilde{\boldsymbol{q}}_{i,j}^{(n)}$, the *k*-space-constrained RPM is applied as in (19), and the associated scattering center point $\hat{v}_{\mathrm{d}}(\tilde{\boldsymbol{q}}_{i,j}^{(n)})$ is obtained.

Step 7: For all τ_i, Steps 2)–6) are repeated, and the k-v_{d} associated point clouds are determined.

Fig. 5 illustrates the processing flow of this method. Note that, in Steps 3 and 4, 4-D FFT and IFFT algorithms can be used to reduce computational complexity. As a distinct advantage over the CI-based method, it avoids unnecessary responses caused by phase uncertainty or interference and also significantly reduces computational complexity by converting the discrete point cloud of $\boldsymbol{q}_{i,j}$ to $\tilde{\boldsymbol{p}}(\boldsymbol{q}_{i,j})$ without connection or tracking procedure.

III. EXPERIMENTAL TEST

A. Setting

This section discusses the experimental validations for each method. This experiment uses the 79-GHz band FMCW MIMO radar, developed by Sakura Tech Corporation. It has a 4.0-GHz frequency bandwidth and a range resolution of 37.5 mm. The real and virtual array configurations of this radar equipment are shown in Fig. 6. The six transmitters and eight receivers with patch array are located on the $y = 0$ mm plane. The horizontal and vertical dimensions of this virtual array are 62 and 4.8 mm, respectively, and the azimuth and elevation angular resolutions are 1.82° and 44.68°. Notably, assuming a distance of 1000 mm to the target, the azimuth and elevation aperture angles are 2.75° and 0.27°, respectively, which is
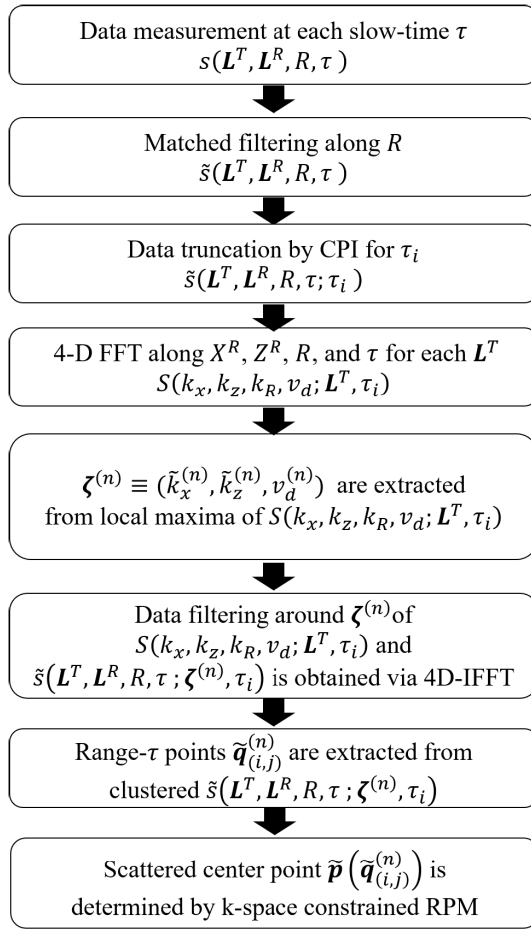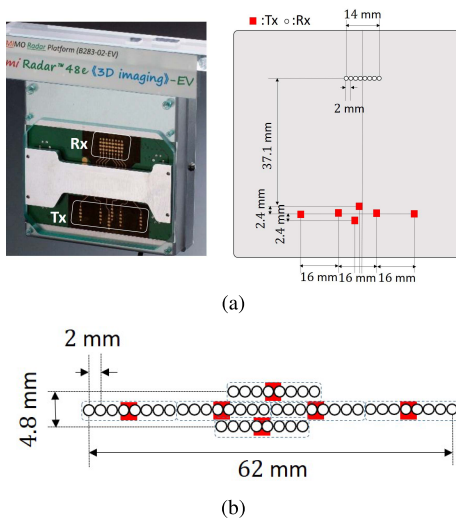
Fig. 5. Flowchart of the proposed method.

Fig. 6. (a) Real and (b) virtual array configurations of 79-GHz band MIMO radar with six transmitters and eight receivers in the experiment.

Fig. 7. Experimental (a) scene and (b) and (c) geometry for three spherical objects with rotating motions.

v_{d} decomposition, indicating the Doppler velocity resolution is 2.47×10^{-3} m/s. The observation time is 7.98 s, and the total number of pulse hits is 1140.

B. Case of Rotating Three Metallic Spheres

1) Results: Range-τ Profile: We now investigate that controlled scenario where the three metallic spheres are rotated at a constant velocity, which enables us to quantitatively validate the accuracy of the target shape, location, and velocity. Notably, the maximum radial velocity of each object is within 0.1 m/s, and the velocity change of the object within this PRI is negligible. The measurement scene and geometrical setup in the anechoic chamber are shown in 7. Each metallic sphere has a 100 mm diameter and is rotated at $2\pi/15$ rad/s on the azimuth table. The distance from each target to the rotation center is 217 mm. The other geometrical conditions are shown in Fig. 7(b) and (c). First, Fig. 8 shows each cross-sectional image of $k_x - k_z - v_{\mathrm{d}}$ responses, responses with the CPI set of the short-time Fourier transform (STFT) to 0.798 s. Due to the higher frequency system, higher Doppler velocity resolution is possible with such a short CPI, namely, high temporal resolution, and the three local maxima on k_x, k_z, and v_{d} are clearly resolved in terms of $k_x - v_{\mathrm{d}}$ spaces, while the resolution along the k_z-direction is lower due to the shorter aperture length along the z-axis. As the filtering process in (13) for the spectra data in Fig. 8 requires the condition that multiple responses are clearly separated more than the resolutions in $k_x - k_z - v_{\mathrm{d}}$ spaces, the performances of the k- and Doppler-velocity decompositions in the proposed

significantly limited to other studies, such as [13], [14], and [36]. A patch antenna has an output power of 10 dBm. The PRI, namely, the sampling interval for the slow time τ, is 7 ms, which corresponds to an unambiguous velocity range of ± 0.141 m/s. The CPI in the STFT process is set to 0.798 s for
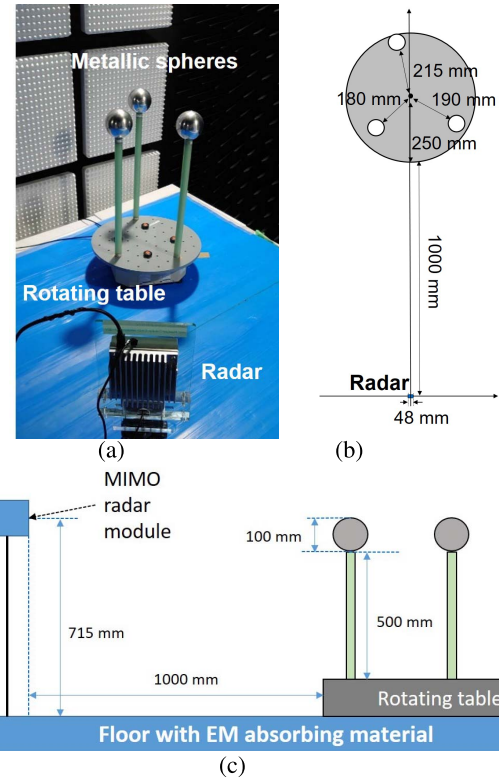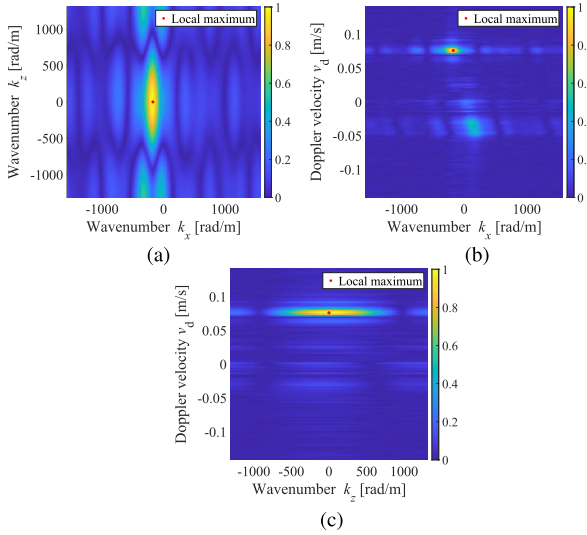
Fig. 8. k_x-k_z-v_d profiles obtained by 4-D FFT process in the proposed method. Red dots denote the extracted local maxima and are processed in data clustering. (a) k_x-k_z, $v_d = 0.0761$ m/s. (b) k_x-v_d, $k_z = 0$ rad/m. (c) k_z-v_d, $k_x = -174.5$ rad/m.

method largely depend on the cross-range and Doppler-velocity resolution, namely, the specification of the FMCW MIMO radar. If the multiple spectra in k- and Doppler-space could not be resolved due to the lack of resolutions, the range-τ point extraction accuracy would be degraded due to interfered or sidelobe effects from multiple objects in the same range resolution gate, resulting in the inaccuracy of the RPM point clouds. In addition, because the object has a rotating motion, there are variances of the Doppler during the assumed CPI, possibly degrading the resolutions of Doppler space, which requires the condition that the filter width in the Doppler velocity ($\Sigma_{v_d} = 0.0143$ m/s) should be sufficiently larger than its resolution (2.47×10^{-3} m/s). In this case, the average SNR is approximately 28 dB. Fig. 8 also shows that a $k_x - k_z - v_d$ conversion can minimize noise components via the CI effect.

Fig. 9 shows the range-τ profiles for the specific combination of the transmitter and the receiver. When employing the "matched filter," (1) and (2) are used, while (12) and (13) are used when employing the "k-v_d Decom." The "k Decom." introduces a similar approach that only considers the k-space direction [26]. In all approaches, the threshold parameter α is 0.1. Focusing on the matched filter responses, there are many unnecessary range-τ points extracted from sidelobe responses, which are also due to multiple reflections being interfered with in the same range resolution at 37.5 mm. In addition, in the case of k-space decomposition, i.e., the method [26], it still retains the inaccuracy associated with insufficient resolution along the k_x-direction, which is an inherent limitation in using a limited array aperture. Note that, if we obtain a much larger aperture size, as in [32] and [33], the RPM point cloud could provide a shape of each target. On the contrary, the k and v_d decompositions produce a more accurate range-τ profile, where the significantly higher Doppler velocity resolution (2.47×10^{-4} m/s) compensates for the lack of azimuth resolution in using only k-space decomposition. However, there are some artifacts in the results
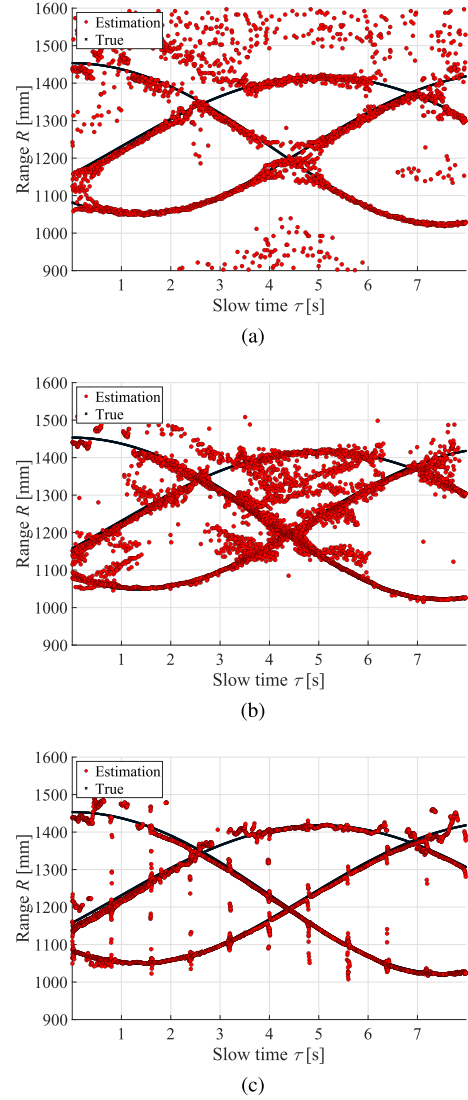

Fig. 9. Range-τ profile at the specific transmitter and receiver combination for the case of three rotating spheres. Black and red dots denote the true and estimation points. (a) Matched filter. (b) k Decomp. (c) $k + v_d$ Decomp.

of Fig. 9(c), which are caused at the specific slow time, corresponding to the start and end times of the STFT process. These errors are caused by the Hamming window process in the STFT process, where the responses at the start and end times are relatively weak, but they could be removed by the sliding window processing. The sliding window approach is one method for eliminating these artifacts; however, it requires a higher computational cost, and it generates redundant range-τ points that overlap over a slow time. Since we assume a short PRI (7 ms), the range-τ points at the start and end time of STFT are not indispensable to recognize a target location or motion, or they can be interpolated by the neighboring range-τ points. Table I summarizes the quantitative error analysis, with an emphasis on the cumulative probability of satisfying different error criteria. This table also demonstrates how the proposed k and v_d decompositions improve the cumulative probability, with over 70 % of the RPs estimated within 10 mm error, which is less than 1/3 of theoretical range resolution (37.5 mm).
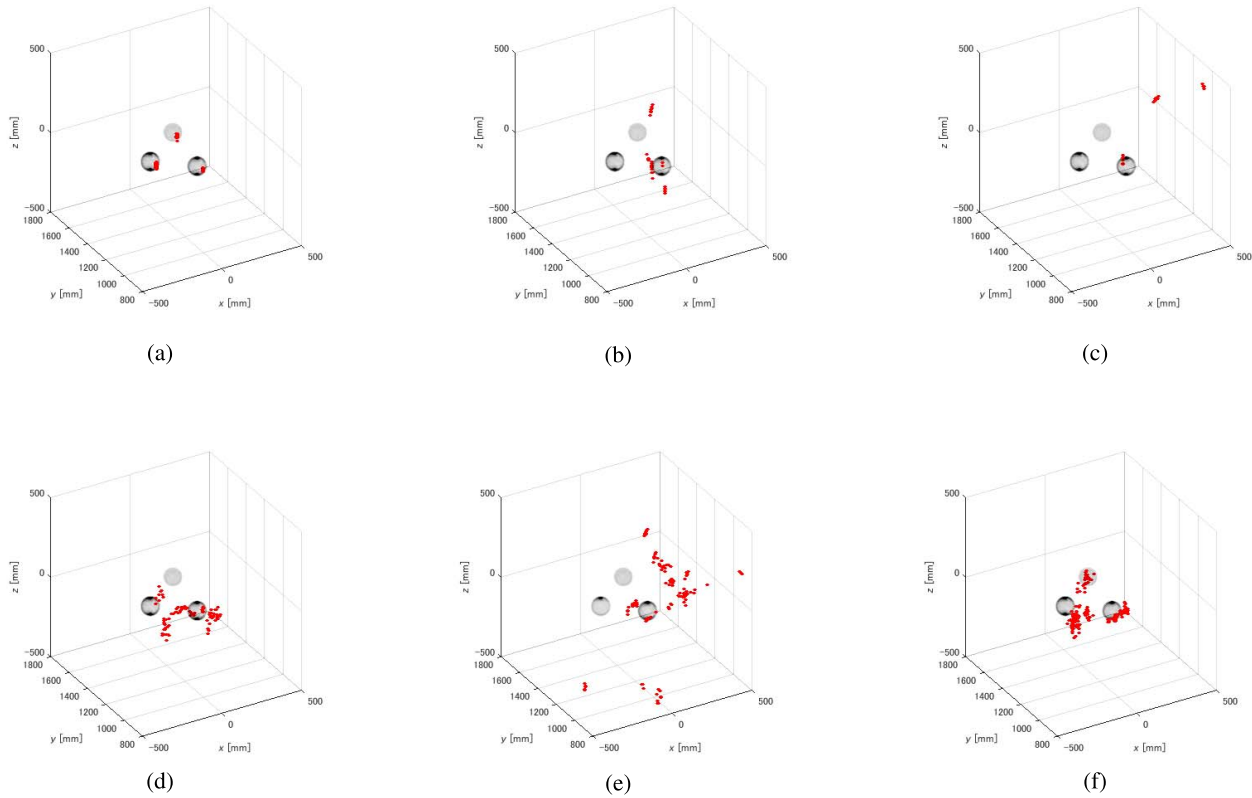
Fig. 10. 3-D reconstruction results by each RPM method. Red dots denote the reconstruction points. (a) Reference. (b) Method I: $\tau = 1$ s. (c) Method II: $\tau = 1$ s. (d) Method III: $\tau = 1$ s. (e) Method IV: $\tau = 1$ s. (f) Method V: $\tau = 1$ s.

TABLE I
CUMULATIVE PROBABILITY OF SATISFYING AS TO R. CASE OF THREE
SPHERICAL OBJECTS WITH ROTATING MOTIONS

	Matched filter	k Decom.	k-v_{d} Decom.
Number of points	193834	238511	396656
$\mathrm{Err}_R \leq 10$ mm	45.0 %	67.6 %	70.7 %
$\mathrm{Err}_R \leq 20$ mm	61.3 %	85.5 %	90.6 %
$\mathrm{Err}_R \leq 50$ mm	68.1 %	93.6 %	96.9 %

TABLE II
DEFINITIONS OF METHODS. THE TERMS "A." AND "N.A" MEAN
"APPLIED" AND "NOT APPLIED," RESPECTIVELY

	$k_X - k_Z$ Decomp.	v_{d} Decomp.	k-space weight
Method I	N. A.	N. A.	N. A.
Method II	A.	N. A.	N. A.
Method III	A.	N. A.	A.
Method IV	A.	A.	N. A.
Method V	A.	A.	A.

TABLE III
PARAMETERS IN EACH RPM METHOD

| Parameter	Values
α	0.1
β	0.1
σ_L	0.1 mm
σ_D	20 mm
σ_ϕ	0.05 rad
σ_θ	0.3 rad
Σ_{k_x}	101 rad/m
Σ_{k_z}	1011 rad/m
Σ_{v_d}	0.0143 m/s

2) Results: Reconstruction Image: Next, Figs. 10 and 11 show the reconstruction results for each RPM-based method at the specific snapshots as $\tau = 1$, 3, 5, and 7 s. We investigated the five imaging methods to confirm the effectiveness of each process, focusing on the k-v_{d} decomposition and the k-weighted RPM scheme as the proposed approach. The definition of each method is shown in Table II. Notably, in

Method I, namely, without using both k or v_{d} decomposition, the matched filter is applied to extract the TOF profiles, i.e., range-τ points. Method V denotes the proposed method, where all k or v_{d} decompositions and k-space weighted schemes are implemented. The parameters used in each RPM are summarized in Table III. Notably, the results entitled "Reference" denotes the case in which the true range-τ, calculated by the actual target shape or location via GO approximation [51], is given in the original RPM method, and these results guarantee that, if the range-τ points are accurately retrieved, the original RPM method would provide accurate 3-D point cloud. As shown by these results, Methods I, II, and IV, namely, using the original RPM without the k-space weight, could not provide a significant localization response for the three objects, even if the k-v_{d} decomposition provides accurate range-τ profiles. This is because the original RPM is extremely
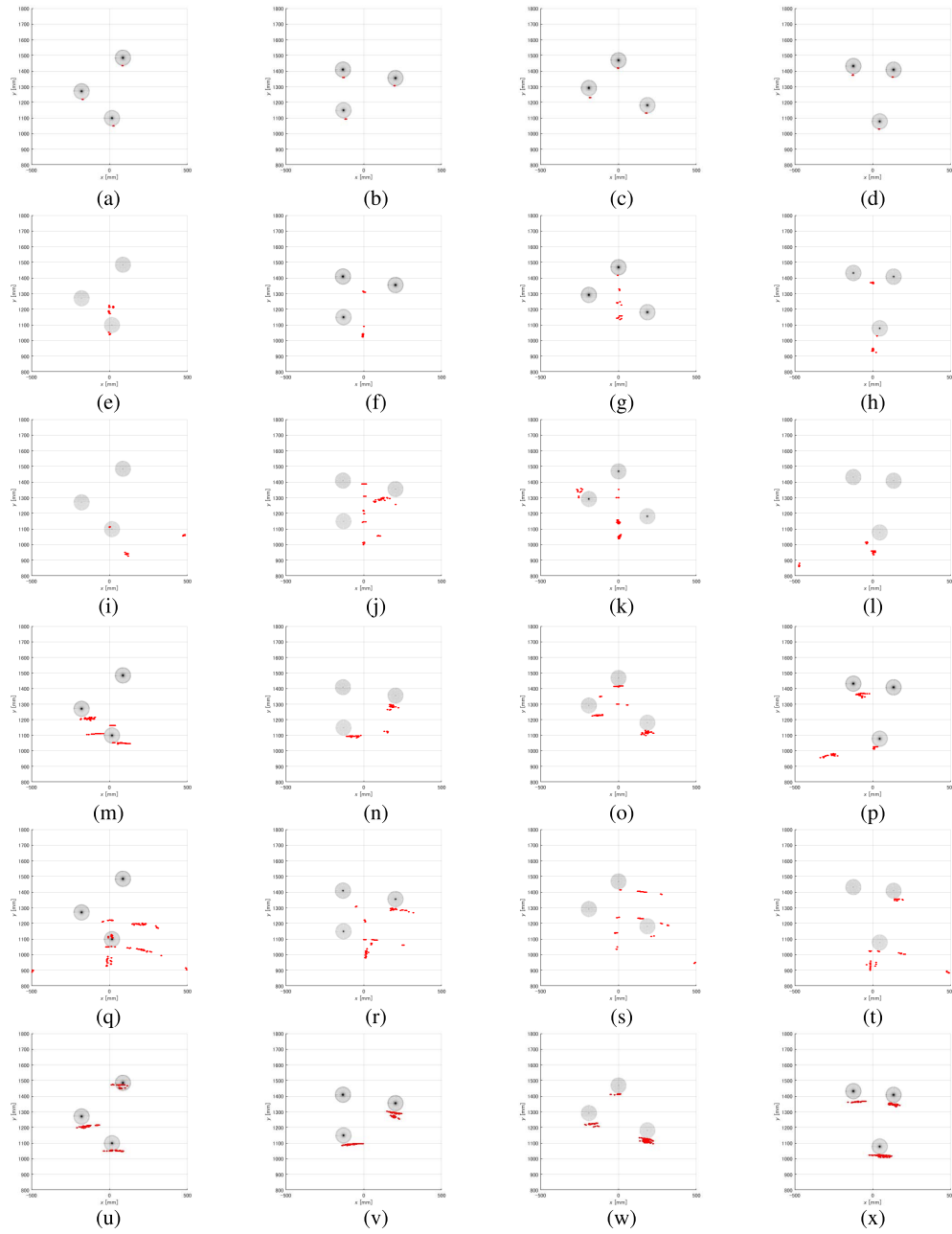
Fig. 11. Projection images on the xy plane, reconstructed by each RPM method. Red dots denote the reconstruction points. (a) Reference: $\tau = 1$ s. (b) Reference: $\tau = 3$ s. (c) Reference: $\tau = 5$ s. (d) Reference: $\tau = 7$ s. (e) Method I: $\tau = 1$ s. (f) Method I: $\tau = 3$ s. (g) Method I: $\tau = 5$ s. (h) Method I: $\tau = 7$ s. (i) Method II: $\tau = 1$ s. (j) Method II: $\tau = 3$ s. (k) Method II: $\tau = 5$ s. (l) Method II: $\tau = 7$ s. (m) Method III: $\tau = 1$ s. (n) Method III: $\tau = 3$ s. (o) Method III: $\tau = 5$ s. (p) Method III: $\tau = 7$ s. (q) Method IV: $\tau = 1$ s. (r) Method IV: $\tau = 3$ s. (s) Method IV: $\tau = 5$ s. (t) Method IV: $\tau = 7$ s. (u) Method V: $\tau = 1$ s. (v) Method V: $\tau = 3$ s. (w) Method V: $\tau = 5$ s. (x) Method V: $\tau = 7$ s.

sensitive to small range-τ profile errors in using quite a small aperture angle (2.75°) or a small number of transmitters and receivers. On the contrary, the k-space-constrained RPM provides more accurate results, as shown in Method III and V. In particular, Method V, using k-v_{d} decomposition, achieves a more reliable localization than Method III, with only k decomposition, and, thus, eliminates a number of points that deviated far from the actual target location. This comparison demonstrates that the k-v_{d} decomposition is effective for the RPM localization scenario. This is because the accuracy of range-τ profile extraction is remarkably enhanced by k-v_{d}

decomposition, whereas the k-space decomposition is influenced by the aperture size. Furthermore, while the resolutions in k_x-k_z space are limited due to the narrow array aperture, a significantly higher Doppler-velocity resolution (2.47×10^{-4} m/s) is available in this case. Thus, by comparing the results of Methods III and V, the above results showed that the decomposition scheme is effective for the post-RPM process not only in k but also in v_{d} space. In addition, although there are some artifacts in range-τ profiles in Fig. 9(c), these artifacts could be eliminated in the final RPM image of Method V because they have relatively lower signal strength

TABLE IV
CUMULATIVE PROBABILITY OF SATISFYING EACH CRITERION IN THE EXPERIMENTAL TEST.
CASE OF THREE SPHERICAL OBJECTS WITH ROTATING MOTIONS

	Number of points	$\text{Err}_{\text{RPM}} \leq 40mm$	$\text{Err}_{\text{RPM}} \leq 70mm$	$\text{Err}_{\text{RPM}} \leq 100mm$	RMSE
True RP (RP is given by GO)	163020	100.0 %	100.0 %	100.0 %	5.3 mm
Method I	76091	14.5 %	22.2 %	32.7 %	418.0 mm
Method II	125568	4.8 %	7.0 %	11.2 %	559.0 mm
Method III	157051	26.2 %	41.4 %	49.7 %	446.64 mm
Method IV	281224	10.6 %	18.2 %	25.6 %	450.5 mm
Method V	318217	51.6 %	73.0 %	79.8 %	280.0 mm

and, hence, should be removed by the RPM thresholding process.

As a quantitative error analysis of the RPM point cloud, the location error Err_{RPM} is defined as

$$\text{Err}_{\text{RPM}} \left(\hat{\boldsymbol{p}} \left(\boldsymbol{q}_{i,j} \right) \right) = \min_{\boldsymbol{p}^{\text{true}}} \| \hat{\boldsymbol{p}} \left(\boldsymbol{q}_{i,j} \right) - \boldsymbol{p}^{\text{true}} \|_2 \qquad (22)$$

where $\hat{\boldsymbol{p}}(\boldsymbol{q}_{i,j})$ represents the locations of the reconstructed RPM point and $\boldsymbol{p}^{\text{true}}$ presents all possible reflection points on the three spherical targets. This error criterion is derived from the fact that each $\hat{\boldsymbol{p}}(\boldsymbol{q}_{i,j})$ could not be assigned to its ground truth position because some points are attributed to noise or other unnecessary responses, such as sidelobe or interfering effects. Then, Err_{RPM} has been used as the standard error criterion of the point clouds, as shown in [25]. Table IV shows the cumulative probability of satisfying the error criteria, in terms of $\text{Err}_{\text{RPM}}(\hat{\boldsymbol{p}}(\boldsymbol{q}_{i,j}))$, and it validates the effectiveness of the proposed method. In this case, the threshold parameters in α and β ($0 \leq \alpha, \beta \leq 1$) are set to 0.1, which should be sufficiently small to detect a response with a low local peak in striking a balance between high detectability and noise or clutter reduction. An appropriate threshold would depend on various parameters for the observation setting, such as array configurations, target shape, location, and numbers, and it is generally difficult to introduce the analytical determination (mathematical procedure) for these parameters. In a real scenario, we could apply a promising thresholding algorithm, such as the constant false alarm rate (CFAR) [52] or Otsu's discriminant analysis [53]. Notably, if a sufficient aperture is available, the RPM-based imaging method can be applied to an extended target, such as the human body or objects with continuous shapes, including an edge or concave area, as demonstrated in [25] and [36]. In such a case, the k-space distribution responses would be expanded; however, the shape of the extended target can be reconstructed by adjusting the filter parameter, as demonstrated in [26], where the filter parameters should be determined by considering the distribution using a nonparametric kernel density estimation method, such as the Gaussian mixture model. In addition, because the proposed preprocessing uses CI and filtering process in k and v_{d} space, random noise, particularly high-frequency components, could be significantly suppressed, as demonstrated in [26], which is based on the k-space decomposition, but the processing for extracting local maxima in (10) is common.

Finally, the CI-based reconstruction is compared with the RPM-based point clouds. The backprojection algorithm is used in the CI reconstruction, which is one of the most accurate CI approaches. The CI images at each slow time point are shown in Fig. 12, with or without introducing the Gaussian weighting functions to suppress the sidelobe effect. They demonstrate that, while the CI approach focuses on the center of the actual target location, it is unable to clearly locate the target surface area. In addition, there are nonnegligible sidelobe responses along azimuth directions without using the weighting function, making it difficult to discriminate between actual and ghost responses from these distributed images. When using the weighting function, it is confirmed that the unnecessary responses due to the coherent process could not be eliminated. In particular, in applying the weighting function, although the sidelobe effect can be suppressed, the cross-range resolution degrades and results in some unnecessary responses at the area that deviates from object positions. While there are several apodizations or signal processing approaches to maintain both sidelobe suppression and resolution abilities, such as [37], [38], [39], [40], [41], and [42], these approaches require specific presumptions, complex signal or array models, or nonlinear optimization processes. On the contrary, the proposed k-v_{d} scheme is based on a simple linear process, and the RPM imaging scheme can avoid the above sidelobe effects because of its incoherent conversion process. It should be noted that, to detect targets from the CI images correctly, some thresholding process is required similar to the RPM-based imaging method, and that is also a critical issue in how to determine the above threshold parameters from the CI distributed image. Even so, the proposed method maintains accuracy for three target localizations [as shown in Fig. 11(f), (l), (r), or (x)]. Neither the RPM nor the CI techniques were able to accurately shape each spherical target, as shown in Figs. 11 and 12. This is because the experimental model assumes a limited array aperture (4.8×62 mm^2) and a target distance of more than 1.5 m, resulting in an approximately 48-mm azimuth resolution and 1170-mm elevation resolution at this distance. These spatial resolutions are obviously insufficient to depict a target shape with a 100 mm diameter. Notably, focusing on the point like target localization, there are so many methods for achieving super-resolution features, such as MUSIC [43], [44], Capon [45], and CS [46], [47], which have been intensively investigated. However, each method has a unique limitation, e.g., the MUSIC inherently suffers from resolution degradation
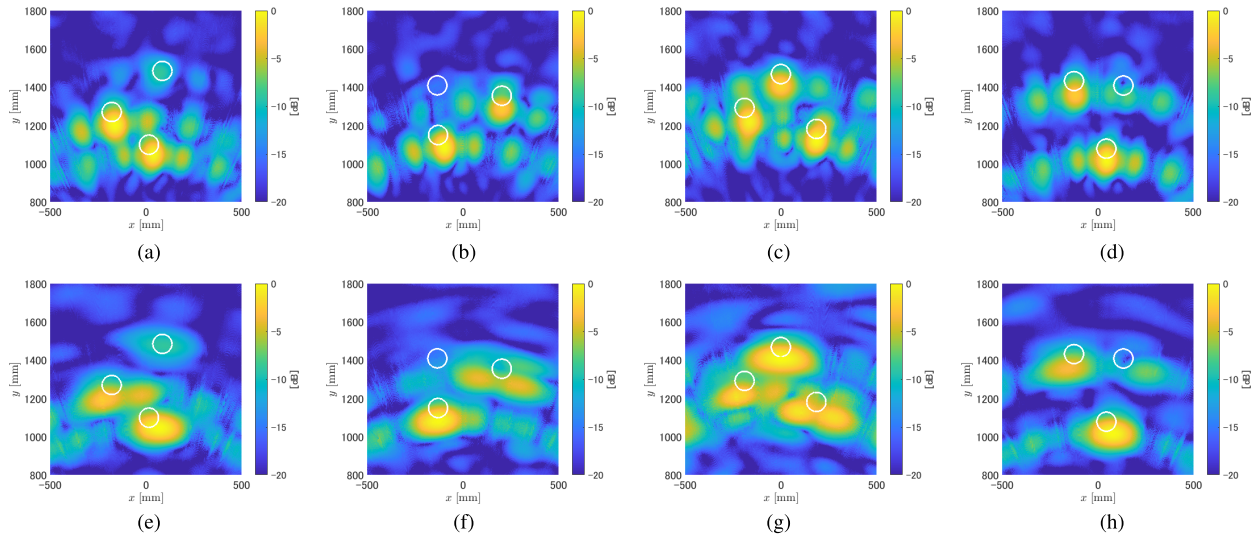
Fig. 12. Cross-sectional reconstruction images on $z = X$ plane, by the backprojection-based CI method. A white hollow circle denotes the actual boundary of spheres. First line: w/o weighting functions. Second line: w/weighting functions. (a) $\tau = 1$ s. (b) $\tau = 3$ s. (c) $\tau = 5$ s. (d) $\tau = 7$ s. (e) $\tau = 1$ s. (f) $\tau = 3$ s. (g) $\tau = 5$ s. (h) $\tau = 7$ s.

TABLE V
AVERAGE COMPUTATIONAL TIME FOR EACH METHOD
REQUIRED AT EACH PULSE HIT

	Range-τ point extraction	RPM	Total
Method I	0.11 s	2.23 s	2.34 s
Method II	54.36 s	3.83 s	58.2 s
Method III	54.36 s	5.85 s	60.2 s
Method IV	5.38 s	8.49 s	13.9 s
Method V	5.38 s	10.36 s	15.8 s

in handling highly correlated signals, such as radar pulses. In addition, they require extremely expensive computational costs because 3-D searches are required in the region of interest in those methods, particularly the CS scheme. On the contrary, the preprocessing of the proposed RPM is based on the 4-D FFT and IFFT data conversion to obtain the desired resolutions along the range axis, which must be much faster than the other methods. Furthermore, the other methods, such as MUSIC, are applicable only to point-like targets, whereas the proposed RPM imaging scheme could be applied to nonpoint-like targets, such as the human body or more complicated target shapes, as demonstrated in [25] and [36]. Note that the array alignment or phase calibration of the radar module could not be perfectly adjusted in this experiment; however, the proposed RPM imaging scheme accurately locates the target positions, even when using such a real radar module. In addition, the range-τ point is extracted from the envelope (magnitude) of the reflection responses [see (2) or (10)], and the phase errors do not significantly affect the accuracy of the range-τ point.

3) Computational Complexity: The computational time of each method is also summarized in Table V, Intel[1] Xeon[1] Silver 4210 CPU @ 2.20-GHz processor with 1024-GB RAM. Here, each total calculation time is averaged with 1140 pulse

[1]Registered trademark.

hits. As shown in Table V, while the range-τ extraction process requires more than 50 s in Method II or III (k-space decomposition), that required in Methods IV and V ($k - v_d$ decomposition) is 5.4 s, that is, ten times shorter. This is because, while the k-space decomposition process requires the decomposition process in each τ, the k-v_d decomposition could remarkably shorten the total processing time using the 4-D FFT process, including the τ-direction. This effect is much eminent in the case that the number of objects is relatively small, i.e., three in this case, because the number of local maxima point as $\zeta^{(n)}$ also becomes small, which reduces the total computational cost. On the other hand, the computational time required for RPM processing in Method III or V, namely, k-space weighted RPM, is relatively larger than that with the original RPM. This increase is caused by the additional calculation process in (20). In addition, in the k decomposition scheme used in Methods II and III, the complexity of the RPM process is much less than that of the decomposition process. More acceleration is needed to implement this method in an actual application scenario, which is our future task to be considered.

4) Sparse Array Results: The reconstruction in the case of sparse array configuration is presented here to verify the advantage of the RPM-based incoherent approach. The reconstruction results obtained by the CI and RPM, in the two cases, are shown in Fig. 13. One case corresponds to the results in Section II-B2, as shown in Figs. 11 and 12, namely, the 6×8 MIMO array is used, where the array spacing of 2 mm satisfies the Nyquist criteria. The other case is that the results obtained from the sparse MIMO array are 6×4, where the array spacing is 4 mm. As shown in this figure, the CI reconstructions result in ambiguous responses to not only the sidelobe but also the grating lobe around the area far from the actual target position in using the sparse array shown in Fig. 13(c), particularly for the area of 800 mm $\leq |x| \leq$ 1100 mm, 0 mm $\leq y \leq$ 500 mm, those of which are difficult to eliminate by using the postprocessing without using any
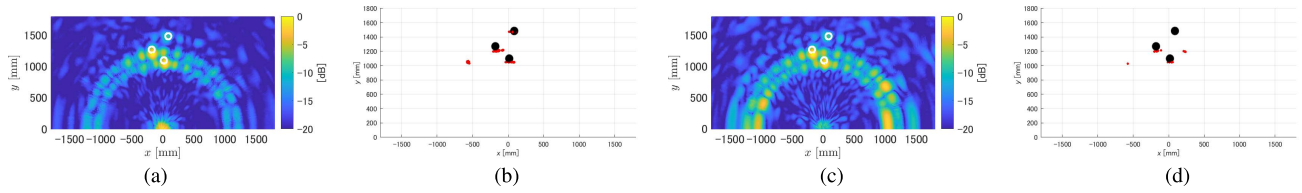
Fig. 13. Comparison between the CI and the proposed RPM-based method (Method V) in each array configuration. (a) CI, 6 × 8 array, $\Delta X_R = 2$ mm. (b) RPM, 6 × 8 array, $\Delta X_R = 2$ mm. (c) CI, 6 × 4 array, $\Delta X_R = 4$ mm. (d) RPM, 6 × 4 array, $\Delta X_R = 4$ mm.
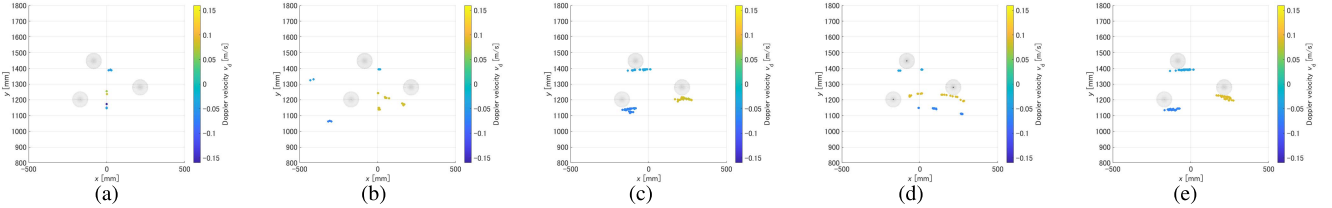

Fig. 14. Doppler velocity-associated RPM localization, where the WKD is applied to each decomposed data. Color dots denote the reconstruction points associated with Doppler velocity. (a) Method I: $\tau = 5$ s. (b) Method II: $\tau = 5$ s. (c) Method III: $\tau = 5$ s. (d) Method IV: $\tau = 5$ s. (e) Method V: $\tau = 5$ s.

prior knowledge of object's location. However, as is the case with RPM localization, it maintains reconstruction accuracy when using such sparse array configurations, as the incoherent process eliminates the effect of phase uncertainty. Although the k-v_d decomposition may suffer from grating or sidelobe effects in a sparse array, the RPM image is free of those effects because it does not use the Fourier or CI schemes in the imaging process. The above point indicates that, even with few elements, the aperture size would be expanded without generating false images, enhancing the RPM imaging area or accuracy. This is why this study recommends the use of RPM when we have no knowledge about target locations. In addition, when dealing with a nonuniform array or unequally sampled data, nonuniform FFT (NUFFT) scheme should be implemented [48], [49]. Thus, like [49] that introduces k-space interpolation using NUFFT, our proposed scheme is also applicable to nonuniformly sampled data.

5) Doppler-Associated Localization: A notable feature of the RPM-based method is the capability for multifunctional localization. In this case, the RPM is incorporated with a Doppler velocity analysis method known as the WKD, which has recently been established to provide an accurate Doppler velocity estimation beyond the limitation between the velocity and temporal resolution [34]. In the WKD, a different study [23] demonstrated that k and v_d decompositions can be applied, considerably enhancing the accuracy of Doppler velocity in each range-τ point. The association between the RPM point cloud and Doppler velocity is very easy because each scattered center $\tilde{p}(q_{i,j})$ is solely associated with the range-τ points, which are also connected to the Doppler-τ point via $\tilde{v}_d(q_{i,j})$. An example of the Doppler associated with an RPM point when the proposed scheme is used is shown in Fig. 14, where the Doppler velocity is determined by the WKD method using k and v_d decompositions. As shown in this figure, while Methods I, II, and IV could not provide an accurate localization or Doppler velocity, Methods III and V, namely, the proposed method, could retain not only an accurate 3-D

point cloud but also an accurately estimated Doppler velocity, associated with each scatter point. To the best of our knowledge, these multifunctional point clouds were not obtained by the CI-based method or other localization schemes. That is another significant advantage of the RPM-based method, i.e., each reconstruction point could be associated with other physical parameters, such as reflection strength, transmitter or receiver locations, and k-space information with one-to-one correspondence. Thus, this method could introduce the k-space weighting in the RPM by using this feature, which is hardly done by the CI-based method due to the data integration process. These multifunction point clouds are expected to upgrade an object recognition performance, such as human body localization or micro-Doppler analysis.

IV. CONCLUSION

This study proposed an accurate 3-D radar localization method, based on RPM point clouds, assuming an mmW MIMO short-range radar with considerably narrow aperture size and angle. To compensate for the lack of accuracy in the incoherent-based RPM approach, a k and v_d space decomposition technique has been implemented as a preprocessing of the RPM range-τ extraction. This decomposition technique efficiently decomposes the spectra data not only by DOA difference but also by Doppler velocity discrimination, which could contribute to suppressing the false detection of range-τ points. In addition, the k-space-constrained RPM suppresses unnecessary divergence of the reconstruction point cloud, which can be accomplished by the RPM's unique feature, that is, the k component can be associated with the scattering center point or range-τ points with one-to-one correspondence. Experiments with the 79-GHz center and 4-GHz bandwidth mmW MIMO radar equipment demonstrated that our proposed method remarkably enhances the reconstruction accuracy of the scattered center points compared with other decomposition schemes or unconstrained RPM algorithms. Notably, when using the 79-GHz band, the traditional CI image cannot

provide sufficient resolution for small objects with a 100 mm diameter. However, the proposed RPM-based method achieves an excellent localization result with such a small aperture size (62 mm × 4.8 mm). This shows that the mmW radar can contribute to the accurate localization of objects up to 100 mm in size, significantly upgrading its applicability.

Although this experiment assumed relatively low-speed objects, in assuming objects with much higher velocity or acceleration, some Doppler velocity compensation methods, such as those in [27] and [28], should be introduced to retain the desired accuracy of this method in the future work. When we assume a narrower bandwidth, e.g., 500 MHz in a 24-GHz band, the advantage of the proposed method becomes clearer because the matched filter-based method would result in inaccurate extraction range-τ points due to the limited range resolution, as demonstrated in [26]. While the simplified spherical targets with a rotating motion have been used to validate their accuracy in a strictly quantitative manner, it is important to validate more realistic targets, such as the human body, as shown in [17].

References

[1] D. A. Andrews, S. W. Harmer, N. J. Bowring, N. D. Rezgui, and M. J. Southgate, "Active millimeter wave sensor for standoff concealed threat detection," *IEEE Sensors J.*, vol. 13, no. 12, pp. 4948–4955, Dec. 2013.

[2] Y. Kim, I. Alnujaim, and D. Oh, "Human activity classification based on point clouds measured by millimeter wave MIMO radar with deep recurrent neural networks," *IEEE Sensors J.*, vol. 21, no. 12, pp. 13522–13529, Jun. 2021.

[3] S. Guo, Q. Zhao, G. Cui, S. Li, L. Kong, and X. Yang, "Behind corner targets location using small aperture millimeter wave radar in NLOS urban environment," *IEEE J. Sel. Topics Appl. Earth Observ. Remote Sens.*, vol. 13, pp. 460–470, 2020.

[4] H. Ng, R. Feger, and A. Stelzer, "A fully-integrated 77-GHz UWB pseudo-random noise radar transceiver with a programmable sequence generator in SiGe technology," *IEEE Trans. Circuits Syst. I, Reg. Papers*, vol. 61, no. 8, pp. 2444–2455, Aug. 2014.

[5] S. B. Yeap, X. Qing, and Z. N. Chen, "77-GHz dual-layer transmit-array for automotive radar applications," *IEEE Trans. Antennas Propag.*, vol. 63, no. 6, pp. 2833–2837, Jun. 2015.

[6] P. J. B. Morris and K. V. S. Hari, "Detection and localization of unmanned aircraft systems using millimeter-wave automotive radar sensors," *IEEE Sensors Lett.*, vol. 5, no. 6, pp. 1–4, Jun. 2021.

[7] J. Song, C. Cui, S. Kim, B. Kim, and S. Nam, "A low-phase-noise 77-GHz FMCW radar transmitter with a 12.8-GHz PLL and a ×6 frequency multiplier," *IEEE Microw. Wireless Compon. Lett.*, vol. 26, no. 7, pp. 540–542, Jul. 2016.

[8] B. Gonzalez-Valdes, Y. Alvarez, S. Mantzavinos, C. M. Rappaport, F. Las-Heras, and J. Á. Martínez-Lorenzo, "Improving security screening: A comparison of multistatic radar configurations for human body imaging," *IEEE Antennas Propag. Mag.*, vol. 58, no. 4, pp. 35–47, Apr. 2016.

[9] S. Gui, J. Li, F. Zuo, and Y. Pi, "Analysis of security imaging method for walking human screening with single channel synthetic aperture radar," *IEEE Access*, vol. 7, pp. 111363–111374, 2019.

[10] F. Soldovieri, A. Brancaccio, G. Prisco, G. Leone, and R. Pierri, "A Kirchhoff-based shape reconstruction algorithm for the multimono-static configuration: The realistic case of buried pipes," *IEEE Trans. Geosci. Remote Sens.*, vol. 46, no. 10, pp. 3031–3038, Oct. 2008.

[11] H. Sun, C. Gao, Z. Zhang, X. Liao, X. Wang, and J. Yang, "High-resolution anisotropic prestack Kirchhoff dynamic focused beam migration," *IEEE Sensors J.*, vol. 20, no. 20, pp. 11753–11760, Oct. 2020.

[12] J. M. Lopez-Sanchez and J. Fortuny-Guasch, "3-D radar imaging using range migration techniques," *IEEE Trans. Antennas Propag.*, vol. 48, no. 5, pp. 728–737, May 2000.

[13] Z. Wang, Q. Guo, X. Tian, T. Chang, and H.-L. Cui, "Near-field 3-D millimeter-wave imaging using MIMO RMA with range compensation," *IEEE Trans. Microw. Theory Techn.*, vol. 67, no. 3, pp. 1157–1166, Mar. 2019.

[14] R. Zhu, J. Zhou, G. Jiang, and Q. Fu, "Range migration algorithm for near-field MIMO-SAR imaging," *IEEE Geosci. Remote Sens. Lett.*, vol. 14, no. 12, pp. 2280–2284, Dec. 2017.

[15] L. Ding, S. Wu, P. Li, and Y. Zhu, "Millimeter-wave sparse imaging for concealed objects based on sparse range migration algorithm," *IEEE Sensors J.*, vol. 19, no. 16, pp. 6721–6728, Aug. 2019.

[16] T. Ohmori and S. Kidera, "Doppler velocity enhanced range migration algorithm for high resolution and noise-robust three-dimensional radar imaging," *IEEE Sensors J.*, vol. 21, no. 18, pp. 20616–20628, Sep. 2021.

[17] Y. Sasaki, F. Shang, S. Kidera, T. Kirimoto, K. Saho, and T. Sato, "Three-dimensional imaging method incorporating range points migration and Doppler velocity estimation for UWB millimeter-wave radar," *IEEE Geosci. Remote Sens. Lett.*, vol. 14, no. 1, pp. 122–126, Dec. 2016.

[18] J. Yang, T. Jin, and X. Huang, "Compressed sensing radar imaging with magnitude sparse representation," *IEEE Access*, vol. 7, pp. 29722–29733, 2019.

[19] M. Miller, J. Hinze, M. Saquib, and A. J. Blanchard, "Adjustable transmitter spacing for MIMO radar imaging with compressed sensing," *IEEE Sensors J.*, vol. 15, no. 11, pp. 6671–6677, Nov. 2015.

[20] F.-F. Gu, Q. Zhang, L. Chi, Y.-A. Chen, and S. Li, "A novel motion compensating method for MIMO-SAR imaging based on compressed sensing," *IEEE Sensors J.*, vol. 15, no. 4, pp. 2157–2165, Apr. 2015.

[21] J. F. Cai, E. J. Candès, and Z. W. Shen, "A singular value thresholding algorithm for matrix completion," *SIAM J. Optim.*, vol. 20, no. 4, pp. 1956–1982, 2010.

[22] J. Wright, A. Ganesh, K. Min, and Y. Ma, "Compressive principal component pursuit," in *Proc. IEEE Int. Symp. Inf. Theory*, Jul. 2012, pp. 1276–1280.

[23] T. Ando and S. Kidera, "Accurate micro-Doppler analysis by Doppler and K-space decomposition for millimeter wave radar," *IEEE J. Sel. Topics Appl. Earth Observ. Remote Sens.*, vol. 15, pp. 2503–2518, 2022.

[24] M. V. R. Manimala, C. D. Naidu, and M. N. G. Prasad, "Convolutional neural network for sparse reconstruction of MR images interposed with Gaussian noise," *J. Circuits, Syst. Comput.*, vol. 29, no. 7, Jun. 2020, Art. no. 2050116.

[25] S. Kidera, T. Sakamoto, and T. Sato, "Accurate UWB radar three-dimensional imaging algorithm for a complex boundary without range point connections," *IEEE Trans. Geosci. Remote Sens.*, vol. 48, no. 4, pp. 1993–2004, Apr. 2010.

[26] Y. Akiyama, T. Ohmori, and S. Kidera, "K-space decomposition-based 3-D imaging with range points migration for millimeter-wave radar," *IEEE Trans. Geosci. Remote Sens.*, vol. 59, no. 8, pp. 6637–6650, Aug. 2021.

[27] L. Xu, J. Lien, and J. Li, "Doppler–range processing for enhanced high-speed moving target detection using LFMCW automotive radar," *IEEE Trans. Aerosp. Electron. Syst.*, vol. 58, no. 1, pp. 568–580, Feb. 2022.

[28] O. Culha and Y. Tanik, "Efficient range migration compensation method based on Doppler ambiguity shift transform," *IEEE Sensors Lett.*, vol. 6, no. 3, pp. 1–4, Mar. 2022.

[29] V. C. Chen and S. Qian, "Joint time-frequency transform for radar range-Doppler imaging," *IEEE Trans. Aerosp. Electron. Syst.*, vol. 34, no. 2, pp. 486–499, Apr. 1998.

[30] Z. Xu, C. J. Baker, and S. Pooni, "Range and Doppler cell migration in wideband automotive radar," *IEEE Trans. Veh. Technol.*, vol. 68, no. 6, pp. 5527–5536, Jun. 2019.

[31] S. S. Ram and A. Majumdar, "High-resolution radar imaging of moving humans using Doppler processing and compressed sensing," *IEEE Trans. Aerosp. Electron. Syst.*, vol. 51, no. 2, pp. 1279–1287, Apr. 2015.

[32] Z. Briqech, S. Gupta, A.-A. Beltay, A. Elboushi, A.-R. Sebak, and T. A. Denidni, "57–64 GHz imaging/detection sensor—Part II: Experiments on concealed weapons and threatening materials detection," *IEEE Sensors J.*, vol. 20, no. 18, pp. 10833–10840, Sep. 2020.

[33] F. Gumbmann and L. Schmidt, "Millimeter-wave imaging with optimized sparse periodic array for short-range applications," *IEEE Trans. Geosci. Remote Sens.*, vol. 49, no. 10, pp. 3629–3638, Oct. 2011.

[34] M. Setsu, T. Hayashi, J. He, and S. Kidera, "Super-resolution Doppler velocity estimation by kernel-based range–τ point conversions for UWB short-range radars," *IEEE Trans. Geosci. Remote Sens.*, vol. 58, no. 4, pp. 2430–2443, Apr. 2020.

[35] T. Hayashi, T. Ando, and S. Kidera, "Three-dimensional Doppler-associated radar imaging method based on bi-directional data processing," *IET Radar, Sonar Navigat.*, vol. 16, no. 1, pp. 145–160, Jan. 2022.

[36] Y. Akiyama and S. Kidera, "Low complexity algorithm for range-point migration-based human body imaging for multistatic UWB radars," *IEEE Geosci. Remote Sens. Lett.*, vol. 16, no. 2, pp. 216–220, Feb. 2019.

[37] R. Zhu, J. Zhou, G. Jiang, B. Cheng, and Q. Fu, "Grating lobe suppression in near range MIMO array imaging using zero migration," *IEEE Trans. Microw. Theory Techn.*, vol. 68, no. 1, pp. 387–397, Jan. 2020.

[38] C. Hu, Z. Chen, X. Dong, and C. Cui, "Multistatic geosynchronous SAR resolution analysis and grating lobe suppression based on array spatial ambiguity function," *IEEE Trans. Geosci. Remote Sens.*, vol. 58, no. 9, pp. 6020–6038, Sep. 2020.

[39] Z. Ding, W. Gao, J. Liu, T. Zeng, and T. Long, "A novel range grating lobe suppression method based on the stepped-frequency SAR image," *IEEE Geosci. Remote Sens. Lett.*, vol. 12, no. 3, pp. 606–610, Mar. 2015.

[40] J. Liu, Y. Jia, L. Kong, X. Yang, and Q. H. Liu, "Sign-coherence-factor-based suppression for grating lobes in through-wall radar imaging," *IEEE Geosci. Remote Sens. Lett.*, vol. 13, no. 11, pp. 1681–1685, Nov. 2016.

[41] Y. Wu, K. Fu, W. Diao, Z. Yan, P. Wang, and X. Sun, "Range sidelobe suppression approach for SAR images using chaotic FM signals," *IEEE Trans. Geosci. Remote Sens.*, vol. 60, pp. 1–15, 2022.

[42] S. Zhou, H. Liu, X. Wang, and Y. Cao, "MIMO radar range-angular-doppler sidelobe suppression using random space-time coding," *IEEE Trans. Aerosp. Electron. Syst.*, vol. 50, no. 3, pp. 2047–2060, Jul. 2014.

[43] J. Zhao, Y. Liu, K. Huo, X. Zhang, and B. Xiao, "A novel high-resolution imaging method using reduced-dimension beamspace unitary MUSIC for OFDM-MIMO radar," *IEEE Access*, vol. 8, pp. 43676–43689, 2020.

[44] B. Li, S. Wang, J. Zhang, X. Cao, and C. Zhao, "Fast randomized-MUSIC for mm-wave massive MIMO radars," *IEEE Trans. Veh. Technol.*, vol. 70, no. 2, pp. 1952–1956, Feb. 2021.

[45] E. Tohidi, A. Hariri, H. Behroozi, M. M. Nayebi, G. Leus, and A. P. Petropulu, "Compressed-domain detection and estimation for colocated MIMO radar," *IEEE Trans. Aerosp. Electron. Syst.*, vol. 56, no. 6, pp. 4504–4518, Dec. 2020.

[46] J. Ding, M. Wang, H. Kang, and Z. Wang, "MIMO radar super-resolution imaging based on reconstruction of the measurement matrix of compressed sensing," *IEEE Geosci. Remote Sens. Lett.*, vol. 19, pp. 1–5, 2022.

[47] M. Rossi, A. M. Haimovich, and Y. C. Eldar, "Spatial compressive sensing for MIMO radar," *IEEE Trans. Signal Process.*, vol. 62, no. 2, pp. 419–430, Jan. 2014.

[48] J. P. Boyd, "A fast algorithm for chebyshev, Fourier, and sinc interpolation onto an irregular grid," *J. Comput. Phys.*, vol. 103, no. 2, pp. 243–257, Dec. 1992.

[49] J. Wang, P. Aubry, and A. Yarovoy, "3-D short-range imaging with irregular MIMO arrays using NUFFT-based range migration algorithm," *IEEE Trans. Geosci. Remote Sens.*, vol. 58, no. 7, pp. 4730–4742, Jul. 2020.

[50] J. Capon, "High-resolution frequency-wavenumber spectrum analysis," *Proc. IEEE*, vol. 57, no. 8, pp. 1408–1418, Aug. 1969.

[51] V. U. Zavorotny and A. G. Voronovich, "Comparison of geometric optics and diffraction effects in radar scattering from steep and breaking waves," in *Proc. IEEE Int. Geosci. Remote Sens. Symp.*, Jul. 2007, pp. 1350–1353.

[52] H. Rohling, "Radar CFAR thresholding in clutter and multiple target situations," *IEEE Trans. Aerosp. Electron. Syst.*, vol. AES-19, no. 4, pp. 608–621, Jul. 1983.

[53] N. Otsu, "A threshold selection method from gray-level histograms," *IEEE Trans. Syst., Man, Cybern. Syst.*, vol. SMC-9, no. 1, pp. 62–66, Jan. 1979.

[54] R. Yamaguchi, S. Kidera, and T. Kirimoto, "3-dimensional imaging and motion estimation method of multiple moving targets for multi-static UWB radar using target point and its normal vector," *IEICE Trans. Commun.*, vol. 97, no. 12, pp. 2819–2829, Dec. 2014.

Takeru Ando received the B.E. degree in communication engineering and informatics from the University of Electro-Communications, Tokyo, Japan, in 2020, where he is currently pursuing the M.E. degree with the Graduate School of Informatics and Engineering.

His research interests include signal processing and imaging for millimeter wave radar and its applications.

Shouhei Kidera (Senior Member, IEEE) received the B.E. degree in electrical and electronic engineering and the M.I. and Ph.D. degrees in informatics from Kyoto University, Kyoto, Japan, in 2003, 2005, and 2007, respectively.

He has been with the Graduate School of Informatics and Engineering, University of Electro-Communications, Tokyo, Japan, since 2009, where he is currently an Associate Professor. He stayed at the Cross-Disciplinary Electromagnetics Laboratory, University of Wisconsin–Madison, Madison, WI, USA, as a Visiting Researcher, in 2016. He has been a Principal Investigator of the PRESTO Program of the Japan Science and Technology Agency (JST) from 2017 to 2021. His current research interest is in advanced radar signal processing or electromagnetic inverse scattering issue for ultrawideband (UWB) 3-D sensor or biomedical applications.

Dr. Kidera is a Senior Member of the Institute of Electronics, Information, and Communication Engineers of Japan (IEICE) and a member of the Institute of Electrical Engineering of Japan (IEEJ) and the Japan Society of Applied Physics (JSAP). He was a recipient of the 2012 Ando Incentive Prize for the Study of Electronics, the 2013 Young Scientist's Prize by the Japanese Minister of Education, Culture, Sports, Science and Technology (MEXT), and the 2014 Funai Achievement Award.